Method to improve the performance of reflectance diffuse optical imaging based on polygonal optical fibers arrangement

Weitao Li (李韪韬), Zhiyu Qian (钱志余)*, and Ting Li (李　婷)

Department of Biomedical Engineering, College of Automation Engineering, Nanjing University of Aeronautics and Astronautics, Nanjing 210016, China

**E-mail: zhiyu@nuaa.edu.cn*

Received December 16, 2008

In order to improve the performance of reflectance diffuse optical imaging (rDOI), a novel polynomial geometry (PG) of optical fibers arrangement is proposed. Polynomial geometry is based on the hexagonal geometry (HG) and multicentered double-density (MD) mode. The overlapping sensitivity matrix, area ratio (AR), reconstruction image, two-absorber model, and contrast-to-noise ratio (CNR) in different depths are used to evaluate the performance of PG. The other three geometries including HG, rectangular geometry (RG), and MD mode are also compared with PG. The deformation of the reconstruction images is evaluted by circular ratio (CR). The results prove that the proposed PG has high performance and minimum deformation in quality of reconstruction image in rDOI.

OCIS codes: 290.7050, 290.1990, 300.1030, 300.2140.

doi: 10.3788/COL20090709.0852.

Diffuse optical imaging (DOI) is a non-invasive technique used to study the changes in concentration of oxygenated and deoxygenated hemoglobin in biological tissue[1−4]. To date, reflectance DOI (rDOI) has been popularly used to study neural activity in the human brain[5−8], breast tumor diagnosis[9,10], and imaging of infant brain[11]. The most widely used instruments for performing rDOI are continuous-wave (CW) ones[12−15]. Compared with time-domain (TD) measurement, the CW ones have low expensive instruments and high spatio-temporal resolution.

A lot of research has been done to improve the spatial resolution of rDOI, of which the overlapping measurement is an important group[16−21]. The rectangular geometry (RG) is the most popular model used in rDOI[18]. The different probe geometries were investigated in Refs. [17,18], and it was concluded that a hexagonal geometry (HG) was the best available options to now. A new multicentered mode was proposed in Refs. [16,21], which was proved with better performance than RG[16]. Three arrangements of probe, including lattice, double-density, and quadruple-density arrangements, were studied in Ref. [20]. All the efforts proved that the overlapping multidistance measurement can improve the image spatial resolution of rDOI by the number and geometry of the sources and detectors.

In this letter, a novel polygonal arrangement of optical fibers with the aim of improving the spatial resolution of rDOI is proposed. In this mode, three sources are placed in an equilateral triangle geometry around the center, and four sources and several detectors are placed as HG. This mode combines HG and multicentered mode into a new arrangement. In order to prove the performance of this mode, the other three arrangements are considered, which are HG, RG, and multicentered double-density (MD) mode with a HG. These three modes have been demonstrated to have the best image quality in rDOI to date. Overlapping sensitivity matrix maps, area ratio (AR), and reconstruction images of four different modes are shown in semi-infinite models. All the results prove that the polygonal optical fibers arrangement can significantly improve the spatial resolution of rDOI.

HG is considered as the best available option because of current technology limitations[18]. So a polygonal geometry (PG) based on hexagonal one is proposed, as shown

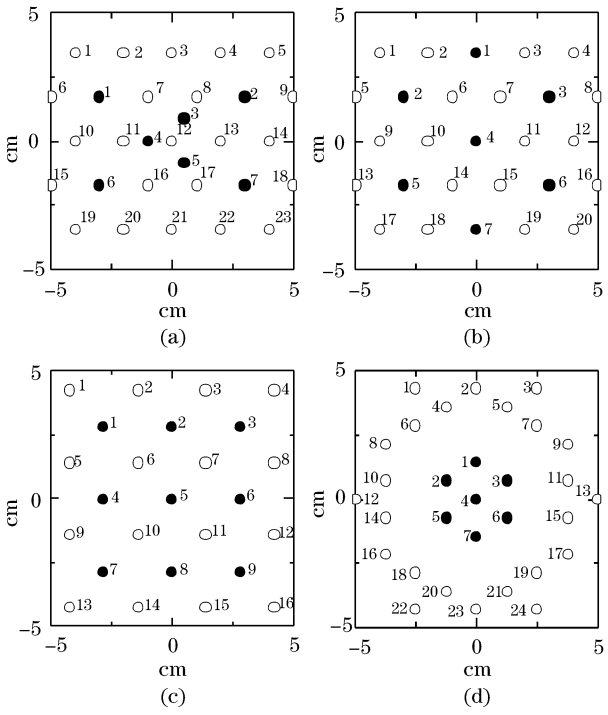

Fig. 1. (a) PG, 7 sources and 23 detectors; (b) HG, 7 sources and 20 detectors; (c) RG, 9 sources and 16 detectors; (d) MD geometry, 7 sources and 24 detectors. The sources and detectors are indicated by dots and open circles, respectively.

in Fig. 1(a). The sources and detectors are indicated by dots and open circles, respectively. The sides of the square region to be explored are 10 cm. Figure 1(a) shows that 4 sources and 23 detectors are placed in HG and the sides of the hexagons are 2.0 cm. Three sources are placed 1.0 cm away from the center in an equilateral triangle geometry. Compared with Refs. [16,18], the PG spanning of 10×8.63 (cm) satisfies the dynamic range requirement.

The other three geometries of optical fibers are also given for comparison. Figure 1(b) shows a HG in which 7 sources and 20 detectors are placed in equilateral HG and the sides of the hexagons are 2.0 cm. Figure 1(c) shows a RG with 9 sources and 20 detectors. The details of the arrangement of Fig. 1(c) can be seen in Refs. [14,22]. Figure 1(d) shows the MD geometry with 7 sources and 24 detectors. The sides of the detectors equilateral hexagons are 5 cm and those for the sources equilateral hexagons are 1.44 cm. The detailed arrangements of other optodes can be seen in Refs. [16,21].

Light propagates through media in a deterministic and predictable way. When it is in highly scattering media (the relationship between absorption ($\mu_{\rm a}$) and reduced scattering coefficients ($\mu'_{\rm s}$) is $\mu_{\rm a} \ll \mu'_{\rm s}$) and not near the source, in time domain it obeys the following diffusion equation:

$$\nabla \cdot D(\mathbf{r})\nabla\Phi(\mathbf{r},t) - v\mu_{\rm a}(\mathbf{r})\Phi(\mathbf{r},t) + vS(\mathbf{r},t) = \frac{\partial\Phi(\mathbf{r},t)}{\partial t}, \quad (1)$$

where $\Phi(\mathbf{r},t)$ is the photon density, v is the speed of light in turbid medium, the photon diffusion coefficient is defined as $D(\mathbf{r}) = v/3(\mu'_{\rm s} + \mu_{\rm a}) \approx v/3(\mu'_{\rm s})$, and $S(\mathbf{r},t)$ is an isotropic source term that provides the number of photons emitted at position $\mathbf{r}$ and time t per unit volume per unit time.

It is hard to get the analysis solution of Eq. (1) directly. The solution for a semi-infinite homogeneous medium for a CW point source is given by[23]

$$\Phi(\mathbf{r}_{\rm s},\mathbf{r}_{\rm d}) = \frac{vS}{4\pi D}\left[\frac{\exp\left(-\sqrt{3\mu'_{\rm s}\mu_{\rm a}}\,|\mathbf{r}_{\rm s}-\mathbf{r}_{\rm d}|\right)}{|\mathbf{r}_{\rm s}-\mathbf{r}_{\rm d}|} - \frac{\exp\left(-\sqrt{3\mu'_{\rm s}\mu_{\rm a}}\,|\mathbf{r}_{\rm s,i}-\mathbf{r}_{\rm d}|\right)}{|\mathbf{r}_{\rm s,i}-\mathbf{r}_{\rm d}|}\right], \quad (2)$$

where $\mathbf{r}_{\rm s}$ and $\mathbf{r}_{\rm d}$ are the positions of source and detector, $\mathbf{r}_{\rm s,i}$ indicates the position of the image source. The semi-infinite boundary condition is satisfied by the imaging method[23].

When the optical properties are spatially varying, one way to find approximate linear solutions is Rytov approximation:

$$\Phi = \Phi_0 \exp(\Phi_{\rm pert}), \quad (3)$$

where Φ is the measured photon density, Φ_0 depends on the background optical properties $\mu_{\rm ao}$ and $\mu'_{\rm so}$, and $\Phi_{\rm pert}$ is linearly related to spatial variations in the optical properties $\delta\mu_{\rm a}$ and $\delta\mu'_{\rm s}$.

Assuming absorption variations only, the formulation of the modified Beer-Lambert law can be used to describe the relationship between the change in optical density, ΔOD, and the change in the absorption coefficient as[17]

$$\Delta{\rm OD}(t,\lambda) = -\ln\left(\frac{\Phi(t,\lambda)}{\Phi_0(\lambda)}\right) = \Delta\mu_{\rm a}(t,\lambda)L(\lambda), \quad (4)$$

where L is the effective average path length of light. Equation (4) can be generalized for a set of discrete volume elements, each having a potentially different absorption change:

$$\Delta{\rm OD}_i(t,\lambda) = \sum_{j=1}^{N_{vox}} \Delta\mu_{{\rm a},j}(t,\lambda)L_{i,j}(\lambda), \quad (5)$$

where $N_{\rm vox}$ means the maximum number of volume elements in images, and i means the ith measurement. Equation (5) can be written in matrix form as

$$\mathbf{y} = \mathbf{A}\mathbf{x}, \quad (6)$$

where $\mathbf{A}$ is the Jacobian (sensitivity) matrix, and $L_{i,j}(\lambda)$ can be derived as

$$L_{i,j}(\lambda) = \Phi_0(r_{\rm s,i}, r_j)\Phi_0(r_j, r_{\rm d,i}), \quad (7)$$

$$\hat{\mathbf{x}} = \mathbf{A}^{\rm T}\left(\mathbf{A}\mathbf{A}^{\rm T} + \alpha s_{\max}\mathbf{I}\right)^{-1}\mathbf{y}, \quad (8)$$

where $\mathbf{I}$ is the identity matrix, $s_{\max}$ is the maximum eigenvalue of $\mathbf{A}\mathbf{A}^{\rm T}$, and α is the regularization parameter (in this letter, α=10^{-6}).

Zhao *et al.* gave the circular ratio (CR) to analyze the shape of the reconstruction image. If the reconstructed regions are not circle, CR cannot be used to evaluate the size of the reconstructed image to the true image. At most situations, we are interested in the size not the shape of the region-of-interest (ROI) compared with the true regions. So in this letter, area analysis is proposed to evaluate the performance of reconstruction. Similar to CR, the area ratio (AR) is defined as

$${\rm AR} = \frac{|A_{\rm true} - A_{\rm rec}|}{A_{\rm true}}, \quad (9)$$

where $A_{\rm true}$ is the area size of the real regions, and $A_{\rm rec}$ is the area size of the reconstruction image. When the AR value is less, the performance of reconstruction image is better. In each reconstructed depth, the AR can be calculated by Eq. (9). In order to evaluate the performance in all depths, the total AR is defined as

$${\rm AR}_{\rm total} = \sum_{i=1}^{\rm Depth} {\rm AR}(i). \quad (10)$$

The contrast-to-noise ratio (CNR) is calculated from the images following the approach outlined by Song *et al.*[24] CNR is plotted as a function of both ROI diameter and the true contrast.

We performed simulations on the overlapping sensitivity matrix maps, area analyses, and the reconstruction images (with segmentation) of PG, HG, RG, MD geometries, respectively.

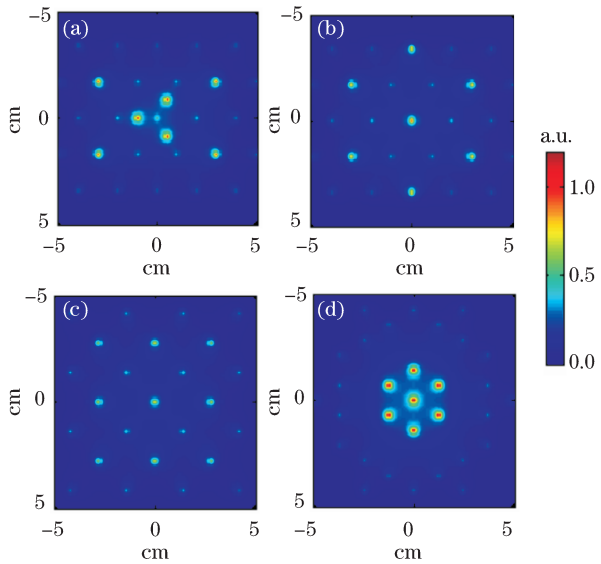

Fig. 2. Overlapping sensitivity matrix maps for (a) PG, (b) HG, (c) RG, and (d) MD geometries.

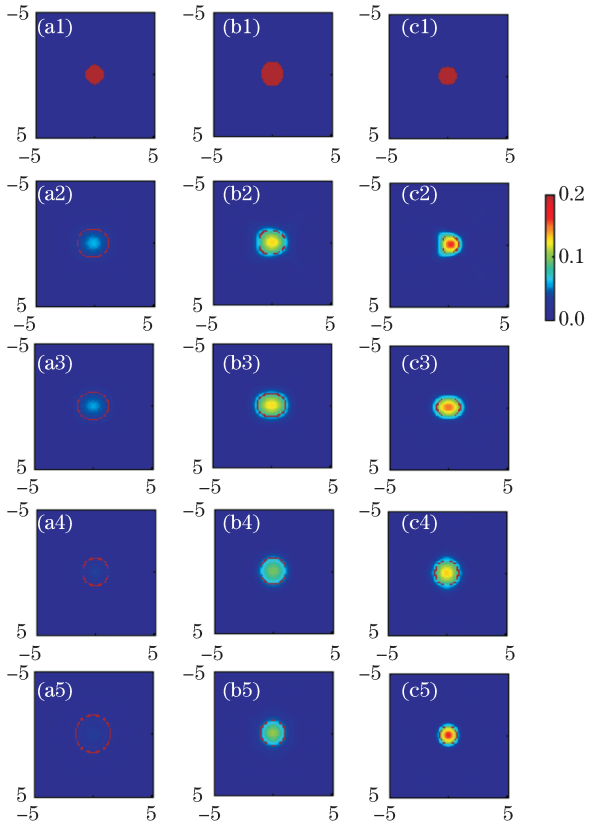

Fig. 3. Real and reconstructed images with absorber's location at (0, 0). From the left, the first column shows the real images, the second, third, fourth, and fifth rows are reconstructed images by PG, HG, RG, and MD, respectively. (a)−(c) correspond to the depths of 2.4, 1.6, and 0.8 cm, respectively. The lines in reconstructed images indicate the objects detected using half-maximum method.

The overlapping sensitivity matrix is the sum of sensitivity matrices of one pair of source and detector. The numbers of sources and detectors are similar with each other, so the difference of overlapping sensitivity matrix measurement maps among four geometries is shown in Fig. 2. The maximum values in overlapping sensitivity matrix maps are 1.05, 0.88, 0.72, and 1.15 for four geometries.

The simulation images for the geometries of PG, HG, RG, and MD are shown in Figs. 3−5. One absorber with $\mu_a = 0.3$ cm^{-1} and $\mu_s' = 10$ cm^{-1} located in the background tissue with $\mu_a = 0.1$ cm^{-1} and $\mu_s' = 10$ cm^{-1} was used for the first two simulations with the results shown in Figs. 3 and 4. The absorber was located at positions of (0, 0) (Fig. 3) and (0, 2 cm) (Fig. 4). Two absorbers located in the region were used for the third simulation, and their positions were (0, 0) and (0, 2 cm), respectively. To our knowledge, it is the first time to use a two-absorber model in the simulation to evaluate the performance of optical fibers arrangement. The radius of absorber was 1.0 cm, and the contrast level was 2.0. Different source depths from the surface of 2.4, 1.6, and 0.8 cm were arranged for simulation. The lines in each reconstructed image indicate the objects detected using the half-maximum method. Then AR defined by Eqs. (9) and (10) was used to evaluate the performance of area size of reconstructed images. The values of AR_{total} according to Figs. 3−5 are given in Tables 1−3.

The CNR was used to evaluate the four geometries. The CNR values are shown in Table 4 at three different depths and the average CNR values are also given for the four geometries.

In the rDOI measurement system, the more sources and detectors are located, the higher spatial resolution can be got. But it is difficult to place more optical fibers in the rDOI because of the limited dynamic ranges of the detectors. The number of sources in the proposed PG is

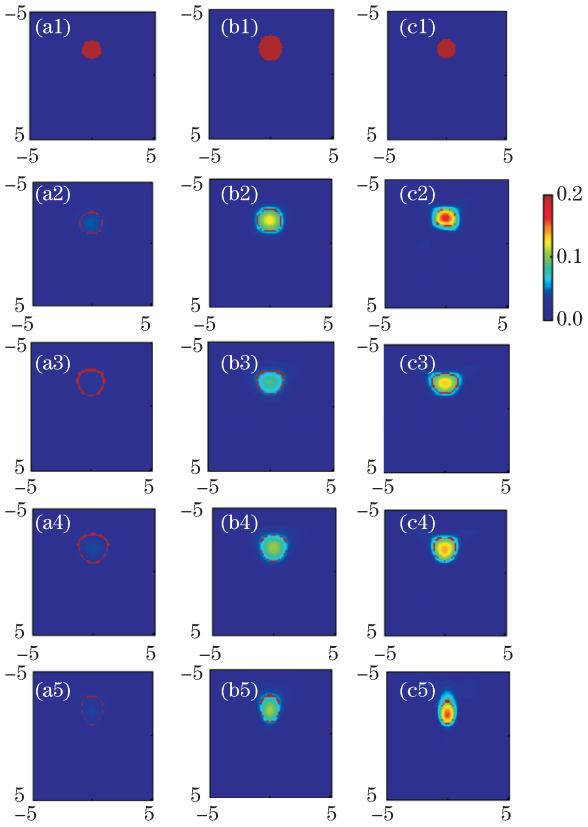

Fig. 4. Real and reconstructed images with absorber's location at (0, 2.0 cm).

equal to that for RG. So the proposed PG can agree the dynamic ranges. From the overlapping sensitivity matrix maps in Fig. 2, we can find the higher sensitivity matrix covers more area of regions in Figs. 2(a)−(c) than in Fig. 2(d), and the area of regions covered in Fig. 2(a) is as much as in Fig. 2(b). Because all the sources were located in the center of the MD, the sensitivity in regions near the center area is high, but in the regions near the boundary the sensitivity is low. So the MD cannot get the high resolution image in all regions, except in the center. On the other hand, the spatial resolution is dependent on the separation between the source and detector. The sensitivity of rDOI drops off exponentially along with the separation. The nearest separation in Figs. 2(a)−(c) is 2.0 cm, and it is 2.5 cm in Fig. 2(d), so the high intensity of light can be detected from source to detectors.

The performance of four geometries can be evaluated directly from the reconstructed images shown in Figs. 3−5. For the one-absorber models located in Figs. 3 and 4, three different depths were given. The real image in Fig. 3(a1) is the same as that in Fig. 3(c1), but the reconstructed images in Figs. 3(a2)−(a5) were blurrier than those in Figs. 3(c2)−(c5). It is all because the different depths. The rDOI has poor depth resolution in deep tissues. The half-maximum method has been used to segment the ROI from background tissue, which is shown by lines in reconstructed images in Figs. 3−5. From the reconstructed lines, the reconstruction image by PG is better than the other three geometries.

In order to evaluate the AR between the real image ROI and reconstructed ROI, AR_{total} was calculated by

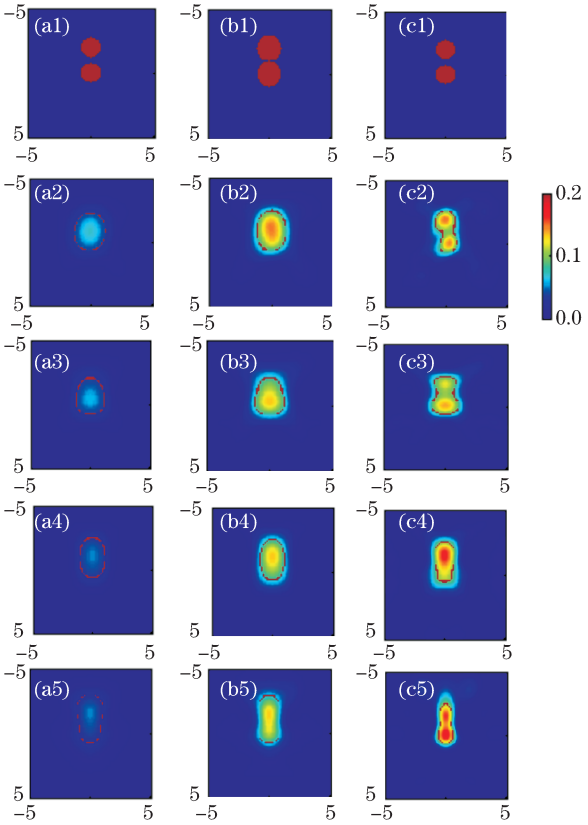

Fig. 5. Real and reconstructed images with absorbers' locations at (0, 0) and (0, 2.0 cm).

Table 1. Region Sizes and Total ARs of Four Geometries in Different Depths Corresponding to Fig. 3

Depth (mm)	Model	Region PG	Size HG	(mm^2) RG	MD
24	197	499	481	393	703
16	317	353	371	385	349
8	197	154	229	313	145
AR_{total}		1.86	1.77	1.80	2.93

Table 2. Region Sizes and Total ARs of Four Geometries in Different Depths Corresponding to Fig. 4

Depth (mm)	Model	Region PG	Size HG	(mm^2) RG	MD
24	197	278	352	393	703
16	317	281	330	385	349
8	197	183	253	313	145
AR_{total}		0.60	1.11	1.71	1.12

Table 3. Region Sizes and Total ARs of Four Geometries in Different Depths Corresponding to Fig. 5

Depth (mm)	Model	Region PG	Size HG	(mm^2) RG	MD
24	394	606	575	558	664
16	634	592	543	512	556
8	394	405	515	409	291
AR_{total}		0.63	0.91	0.65	1.07

Table 4. CNR and Average CNR Values of Four Geometries in Different Depths (Locations at (0, 0) and (0, 2.0 cm))

Depth	PG	HG	RG	MD	PG	HG	RG	MD
(mm)	(0, 0)				(0, 2.0 cm)			
24	6.34	6.48	6.71	4.96	6.25	6.0	6.37	7.34
16	7.58	7.26	6.88	7.72	7.32	6.49	7.08	7.65
8	8.71	8.66	7.49	11.4	9.13	8.08	8.43	7.27
Average	7.54	7.47	7.03	8.02	7.57	6.86	7.29	7.42

Table 5. CR_{depth} Values of Four Geometries in Different Depths (Locations at (0, 0) and (0, 2.0 cm))

Depth	PG	HG	RG	MD	PG	HG	RG	MD
(mm)	(0, 0)				(0, 2.0 cm)			
24	1.14	1.13	0.76	1.79	0.31	0.72	0.86	0.62
16	0.17	0.37	0.23	0.23	0.09	0.20	0.22	0.23
8	0.16	0.48	0.62	0.17	0.24	0.30	0.31	0.48
All-CR_{depth}	1.47	1.98	1.61	2.19	0.64	1.22	1.39	1.33

Eq. (10) and shown in Tables 1 and 2. Previously, the performance was only discussed in one depth. We evaluated the performance of four geometries by combining three representative depths together. So the AR_{total} was got by adding all the AR values in different depths. From Table 1, the AR_{total} of PG is as much as that in all other geometries; while in Table 2, the AR_{total} of PG is smaller than others.

The two-absorber model was proposed to evaluate the performance of rDOI. We attempted to analyze the performance of reconstructed images. The first important thing is to distinguish the two different ROIs, which is not the same as one-absorber model. From Fig. 5, only the reconstructed images of PG can be used to segment two ROIs. With the depth deeper and deeper, the distinguishability is lower and lower. The second index is AR_{total}. As shown in Table 3, the AR_{total} of PG is the best in four geometries. Because the lightnesses in the reconstructed images are not the same when the absorbers are at (0, 0) and (0, 2.0 cm), if different values not the half-maximum ones are used to segment the ROI, better lines can be got. How to select the value is out of the purpose of this letter.

We evaluate the CNR at different depths and use the average CNR to evaluate the performance of optical fibers arrangement. From Table 4, the PG and MG are the best two of the four geometries. When the absorber is in the center, the CNR of MG is better. The reason is that all the sources are put around the center. When the absorber is in the position (0, 2.0 cm), the CNR of the proposed PG is better. The reason is that the sources are put more uniform in the ROI. PG is better than MG with the combined consideration of CNR and AR analyses.

The proposed optical fibers layout is an asymmetric arrangement. So CR is used to evaluate the deformation of reconstruction images[16]. CR is given by

$$\mathrm{CR} = \frac{R_{\mathrm{real}} - R_{\mathrm{rec}}}{R_{\mathrm{real}}}, \tag{11}$$

where R_{real} is the radius of the real images, and R_{rec} is the radius of the reconstruction images. With R_{recx} and R_{recy} being the radii of the reconstruction images corresponding to x-axis and y-axis, respectively, CR_x and CR_y can be calculated accordingly. At one depth we define $\mathrm{CR}_{\mathrm{depth}} = |\mathrm{CR}_x| + |\mathrm{CR}_y|$, then we add $\mathrm{CR}_{\mathrm{depth}}$ at different depths (all-$\mathrm{CR}_{\mathrm{depth}}$) to evaluate the deformation of the optical fibers layout. The values of $\mathrm{CR}_{\mathrm{depth}}$ and all-$\mathrm{CR}_{\mathrm{depth}}$ are shown in Table 5. We can find that the all-$\mathrm{CR}_{\mathrm{depth}}$ values of objects in two different positions of PG are the best, which means that the deformation of the objects of PG is the minimum.

In conclusion, a novel polygonal arrangement of optical fiber is presented. The proposed PG geometry combines the optical fiber arrangements of HG and MD into one. It can agree the dynamic ranges much better compared with the other three geometries. From the reconstruction images in different depths and evaluation of AR_{total} and CNR, the high performance of rDOI can be got by the proposed geometry.

This work was supported by the National Natural Science Foundation of China (No. 30671997) and the National "863" Program of China (No. 2008AA02Z438).

References

1. G. Themelis, H. D'Arceuil, S. G. Diamond, S. Thaker, T. J. Huppert, D. A. Boas, and M. A. Franceschini, J. Biomed. Opt. **12,** 014033 (2007).
2. J. Selb, D. K. Joseph, and D. A. Boas, J. Biomed. Opt. **11,** 044008 (2006).
3. N. Cao and A. Nehorai, Opt. Express **15,** 896 (2007).
4. P. K. Yalavarthy, B. W. Pogue, H. Dehghani, and K. D. Paulsen, Med. Phys. **34,** 2085 (2007).
5. J. P. Culver, A. M. Siegel, J. J. Stott, and D. A. Boas, Opt. Lett. **28,** 2061 (2003).
6. L. Dai, Z. Qian, K. Li, T. Yang, and H. Wang, J. Biomed. Opt. **13,** 044003 (2008).
7. S. Chen, F. Feng, P. Li, S. L. Jacques, S. Zeng, and Q. Luo, J. Biomed. Opt. **11,** 034002 (2006).
8. A. P. Gibson, T. Austin, N. L. Everdell, M. Schweiger, S. R. Arridge, J. H. Meek, J. S. Wyatt, D. T. Delpy, and J. C. Hebden, NeuroImage **30,** 521 (2006).
9. E. L. Heffer and S. Fantini, Appl. Opt. **41,** 3827 (2002).
10. C. Zhu, G. M. Palmer, T. M. Breslin, J. Harter, and N. Ramanujam, Lasers in Surgery and Medicine **38,** 714 (2006).
11. T. Vaithianathan, I. D. C. Tullis, N. Everdell, T. Leung, A. Gibson, J. Meek, and D. T. Delpy, Rev. Sci. Instrum. **75,** 3276 (2004).
12. A. Shirkavand, S. Sarkar, M. Hejazi, L. Ataie-Fashtami, and M. R. Alinaghizadeh, Chin. Opt. Lett. **5,** 238 (2007).
13. J. Wang, G. Wang, and Z. Xu, Chin. Opt. Lett. **6,** 530 (2008).
14. J. Selb, A. M. Dale, and D. A. Boas, Opt. Express **15,** 16400 (2007).
15. G. Ma, J.-F. Delorme, P. Gallant, and D. A. Boas, Appl. Opt. **46,** 1686 (2007).
16. Q. Zhao, L. Ji, and T. Jiang, J. Biomed. Opt. **11,** 064019 (2006).
17. D. A. Boas, A. M. Dale, and M. A. Franceschini, NeuroImage **23,** S275 (2004).
18. D. A. Boas, K. Chen, D. Grebert, and M. A. Franceschini, Opt. Lett. **29,** 1506 (2004).
19. J. P. Culver, V. Ntziachristos, M. J. Holboke, and A. G. Yodh, Opt. Lett. **26,** 701 (2001).
20. T. Yamamoto, A. Maki, T. Kadoya, Y. Tanikawa, Y. Yamada, E. Okada, and H. Koizumi, Phys. Med. Biol. **47,** 3429 (2002).
21. Q. Zhao, L. Ji, and T. Jiang, Opt. Express **15,** 4018 (2007).
22. R. J. Gaudette, D. H. Brooks, C. A. DiMarzio, M. E. Kilmer, E. L. Miller, T. Gaudette, and D. A Boas, Phys. Med. Biol. **45,** 1051 (2000).
23. D. A. Boas, J. P. Culver, J. J. Stott, and A. K. Dunn, Opt. Express **10,** 159 (2002).
24. X. Song, B. W. Pogue, S. Jiang, M. M. Doyley, H. Dehghani, T. D. Tosteson, and K. D. Paulsen, Appl. Opt. **43,** 1053 (2004).